

Project Final Report

Xuxiao Li, April 28, 2020

The github repository for the project is:

https://github.com/xuxiaoli1993/machine_learning_final_project.git.

1 Introduction

In laser-based metal processing techniques, a laser is illuminated on the metal material to provide heating of the metal and achieve desired effects. Commonly, the metal is melted upon the intensive heating and even become vaporized when a large heat input is sometimes desired (e.g., in some laser metal welding and laser-based 3D printing processing conditions). When the vaporization occurs, the metal vapor exerts a recoil pressure on the molten metal, which forms a depression region at the molten pool. This depression region, referred to as the keyhole, can have non-uniform laser absorption on its surface, which then triggers the hydrodynamic instability of the keyhole [1]. The keyhole instability has been identified as one of the most important mechanisms for the formation of pores (porosity defects) and is an active research area [2–4]. A experimental observation of the keyhole instability is shown in Fig. 1.

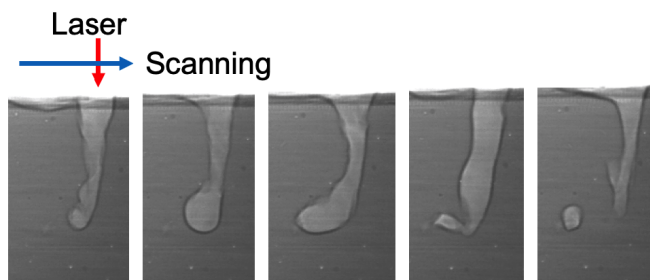


Figure 1: Keyhole instability observed by X-ray high speed imaging. A time sequence of five captures are shown. The red arrow indicates the laser where it is illuminated on a bare metal plate. The laser is scanning from left to right. A pore is observed at the last time frame due to the keyhole instability.

Due to the difficulties of extracting quantitative information from direct experimental observations of the keyhole instability, multiphysics simulations are a supplement to enable quantitative understanding of the complex phenomenon. An exemplary result from such a simulation is shown in Fig. 2. The multiphysics models typically utilize the ray-tracing method to calculate the laser absorption distribution on the keyhole surface. Thereafter, the subsequent keyhole dynamics can be simulated with computational fluid dynamics techniques. The absorption calculation is the prerequisite for the subsequent simulations and is crucial to ensure the physical fidelity of the multiphysics models.

In the ray-tracing method to calculate the laser absorption, the laser is discretized into a large amount of ray bundles. Each ray bundle is fired towards the keyhole surface and reflects according to the geometric optics upon incidence on the keyhole surface. Each ray bundle is explicitly traced until most of its power has been absorbed or it leaves the calculation domain. This physics-based method is of high accuracy but can be computationally costly when the amount of ray bundles need to be very large (especially in three-dimension) to ensure consistent result.

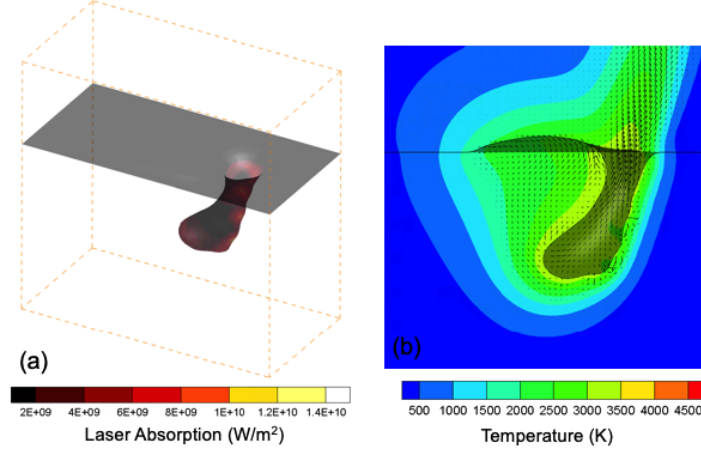


Figure 2: A multiphysics simulation result for keyhole dynamics. (a) shows a three-dimensional keyhole with the laser absorption distribution flooded on the keyhole surface. (b) shows a cross section of the 3D simulation where the temperature contour and the fluid flow in both metal and gaseous phase are displayed. It is noted that the multiphysics simulation can reveal more quantitative information regarding the keyhole dynamics.

The objective of this project is to use machine learning techniques to accelerate the computation of laser absorption on the keyhole surface. The training and testing data can be obtained from the physics-based, ray-tracing simulations where the keyhole shape is treated as the “feature” and the laser absorption on the keyhole surface is the “label”. By combining both physics-based and data-driven modeling techniques, the keyhole dynamics can be simulated with less computational time.

2 Problem Definition

For this project, the three-dimensional (3D) keyhole geometry is simplified to two-dimension to first investigate the feasibility of applying machine learning techniques to predict laser absorption. A typical two-dimensional (2D) keyhole shape can be obtained by extracting a slice from the 3D simulations, as shown in Fig. 3a. The keyhole shape can be implicitly represented by the level-set function. The level-set function is defined as the signed distance to the keyhole surface. As shown in Fig. 3b, the region above the keyhole surface has positive level-set, the region below the keyhole surface has negative level-set, and the zero-level-set contour implicitly captures the keyhole surface. Based on the level-set field, a 2D ray-tracing simulation is run to calculate the 2D laser absorption as shown in Fig. 3c.

In the 2D setup, the machine learning task can be stated as follows. Given a 2D array (or equivalently an image) of the level-set field such as in Fig. 3b, find the 2D array (image) of the laser absorption distribution such as in Fig. 3c. It is noted that the 2D array for the laser absorption is sparse, as only in the region near the keyhole surface is the laser absorption non-zero. This machine learning task can be viewed as a image-to-image regression problem: given the level-set “image” ϕ , find the absorption “image” Q .

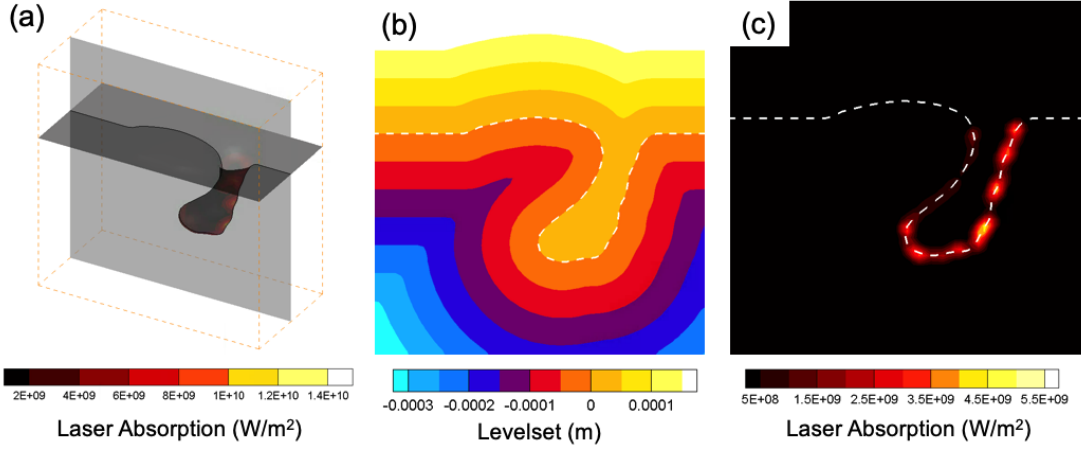


Figure 3: 2D simplification of the keyhole geometry. (a) A 2D slice is extracted from the simulated 3D keyhole. (b) The level-set function on the extracted slice. (c) The 2D laser absorption distribution based on the 2D level-set field (b); this is calculated by conducting a 2D ray-tracing simulation. Notice that the white-dashed line in (b) and (c) is the zero-level-set contour.

3 Method

3.1 Data Collection

A total of 8 full simulations of 3D keyhole dynamics with different settings of laser power and scanning speed (setup resembling Fig. 1) are conducted. From each 3D simulation, slices are extracted at multiple time frames, and a total of 1490 slices are extracted. Then, for each extracted slice, a 2D ray-tracing simulation is run to obtain the 2D absorption based on the 2D level-set field of the slice. The 1490 pieces of data is split into the training set (90 %) and the testing set (10 %). The 1341 (90 %) pieces of data, $S = \{(\phi_i, Q_i), i = 1 \cdots m, m = 1341\}$, constitutes the training set in the current project. The rest 149 (10 %) of the data is the testing set which is blind to the machine learning algorithm during training. The data ϕ_i and Q are both 2D arrays with a size of 60×60 .

3.2 Data Preprocessing

The performance of machine learning algorithms can be highly dependent on the preprocessing of the data set. It is noticed in Fig. 2c that the absorption distribution is sparse. With a such a “discontinuous” distribution, the machine learning algorithm needs to not only predict the accurate absorption value but also pinpoint where the absorption is located. In practice, it is found that accuracy of predicting such a discontinuous distribution is often insufficient. To overcome this difficulty, the original absorption distribution is constantly extrapolated from the keyhole surface towards the bulk regions, as shown in Fig. 4. The extrapolated absorption field is smoother and is practically proved to significantly improve the accuracy of the machine learning algorithms. The data set is represented as (ϕ_i, Q_i^{ext}) after the extrapolation trick.

It is also desirable to normalize the data set such that all the data values are around 1.0. The normalization factors of $\phi_{\text{norm}} = 0.0004$ and $Q_{\text{norm}} = 10^{10}$ are selected, and the normalized data set is denoted as $(\bar{\phi}_i, \bar{Q}_i^{ext})$.

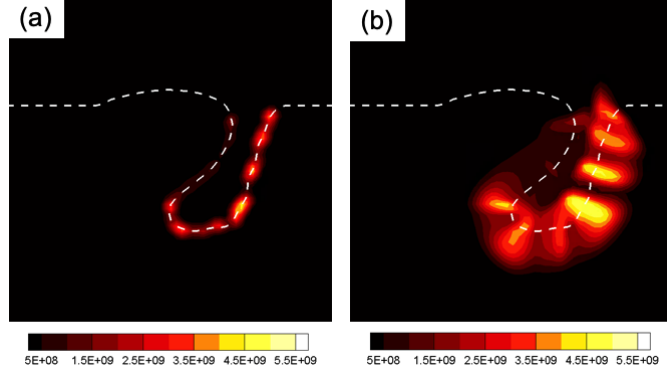


Figure 4: Extrapolation trick to enhance the accuracy of machine learning algorithms. (a) the original discontinuous (sparse) distribution of laser absorption. (b) The extrapolated absorption field.

3.3 Metrics

The performance of the machine learning algorithm is benchmarked by the root mean squared (RMS) error. However, due to the extrapolation trick, only the indices (i, j) near the keyhole surface should be compared between the prediction and the ground truth. Therefore, the average prediction RMS error for a given set of examples can be written as:

$$\text{RMS} = \frac{1}{n} \sum_{k=1}^n \sqrt{\frac{1}{C_k} \sum_{\substack{(i,j) \in \\ \text{keyhole} \\ \text{surface}}} (\bar{Q}_{ij,\text{pred}}^{\text{ext}} - \bar{Q}_{ij,\text{true}})^2}$$

Here, n is the number of examples in the set, and C_k is the number of indices (i, j) within the keyhole surface region for the k^{th} example. It is noted that the normalized absorption is compared between the prediction and the ground truth. The predictions are the extrapolated absorption while the ground truth is the original absorption. However, the two would be the same when only the indices (i, j) within the keyhole surface region is accounted for.

3.4 Convolutional Neural Network

The convolutional neural network (CNN) is selected as the machine learning algorithm to learn the laser absorption from the level-set function in the current project. The CNN is selected due to its advantages to recognize and extract features in an image. Here, the keyhole shape (represented by the level-set field) can be viewed as an image, and it is the geometric features of the keyhole that determines its absorption distribution. The strategy of constructing neural network is as follows. CNN layers are first implemented to extract those features; after that, dense (or fully connected) layers are implemented to correlate those features with the absorption distribution.

The architecture of the neural network is summarized in Fig. 5. Three CNN blocks are used to extract features of the level-set field input. Each block consists of a convolutional layer followed by a max-pooling layer with of size of 2. A dropout layer with a rate of 0.25 is used after the CNN blocks to alleviate overfitting. Then, the features learned from CNN blocks are flattened to one-dimensional (1D) arrays to feed into the dense layers. The first dense layer has 256 nodes while the last dense layer has 3600 nodes to represent the 60×60 2D array. Finally, the output from the dense layers is reshaped to a 2D array as the absorption distribution. All the activation functions except the last dense layer are ReLU functions. The last layer has a linear activation function due to the regression nature of the current problem. The neural network is implemented

with tensorflow keras and run on the GPU nodes at the center of high performance computing of University of Utah.

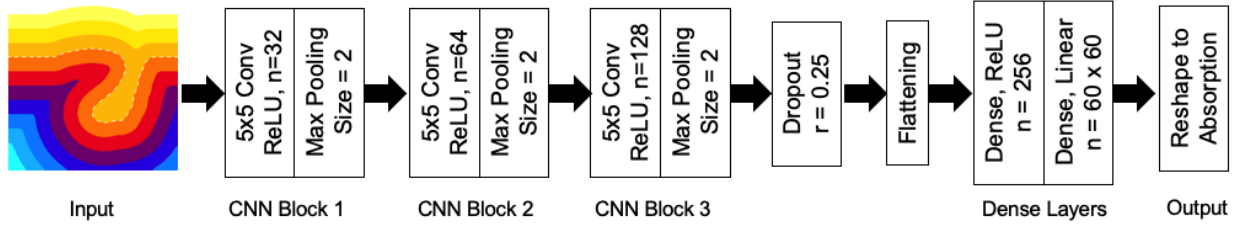


Figure 5: Architecture of the neural network.

3.5 Hyperparameter Tuning

There is a large amount hyperparameters in the neural network shown in Fig. 5. They are the number of convolutional and dense layers, the filter number and kernel size at each convolutional layer, the number of nodes at each dense layer (except the last dense layer), the rate of the dropout layer, and the number of epochs during training. The bootstrapping method is used to benchmark these hyperparameters, as described as follows.

For each bootstrapping cycle, a new training set and a validation set are sampled with replacement from the original training set with 1341 pieces of data. The number of examples in the new training set and validation set are 80 % and 20 % of the original 1341 pieces of training data, respectively. Then, the neural network is trained based on the new training set. For each epoch during the training process, the RMS error is computed for the validation set, and the training is forced to stop when the RMS error does not significantly decrease with increasing number of epochs. A total of 5 cycles are conducted and the average number of epochs will be adopted to train the original training set and compare with the testing set which is blind to the entire training process. The average of RMS error of validation set from the 5 bootstrap cycles will be used as the metric to evaluate the accuracy for a certain combination of hyperparameters. The architecture given in Fig. 5 is selected as it achieves relatively small average RMS error from the bootstrapping cycles.

4 Results and Discussion

The performance of the neural network is demonstrated in Fig. 6 where the predictions of the testing examples are compared with the corresponding truth absorption. The first column shows the level-set field which are the inputs of the neural network. The second column highlights the positive and negative level-set values to better visualize the keyhole boundary. The third and fourth columns are the true and predicted absorption distribution on the keyhole surface. It is noted that the extrapolated absorption is actually predicted, but only the absorption near the keyhole surface is shown in Fig. 6 for visualization purposes. Also, both the level-set and absorption shown in Fig. 6 are the normalized ones as described previously. The average RMS error for the training set is ~ 0.0613 and for the testing set is ~ 0.0656 .

As can be seen in Fig. 6, the predictions from the neural network can not only recognize the general keyhole shapes but also the detailed kinkiness on the keyhole surface (e.g., the second row). The magnitude of the predicted absorption also closely matches with the ground truth, as indicated by the brightness in the third and fourth column and also the small average RMS errors. A slight overfitting is observed which indicates possible better hyperparameters can be found. However, practical experience from the tedious hyperparameter tuning process suggests that the

improvement on the fine-tuning should be limited. Compared to fine-tuning of hyperparameters, the extrapolation trick described previously more significantly improves the RMS error. Generally, the current accuracy of absorption is deemed acceptable as the input to the subsequent fluid dynamics simulations for the keyhole behavior.

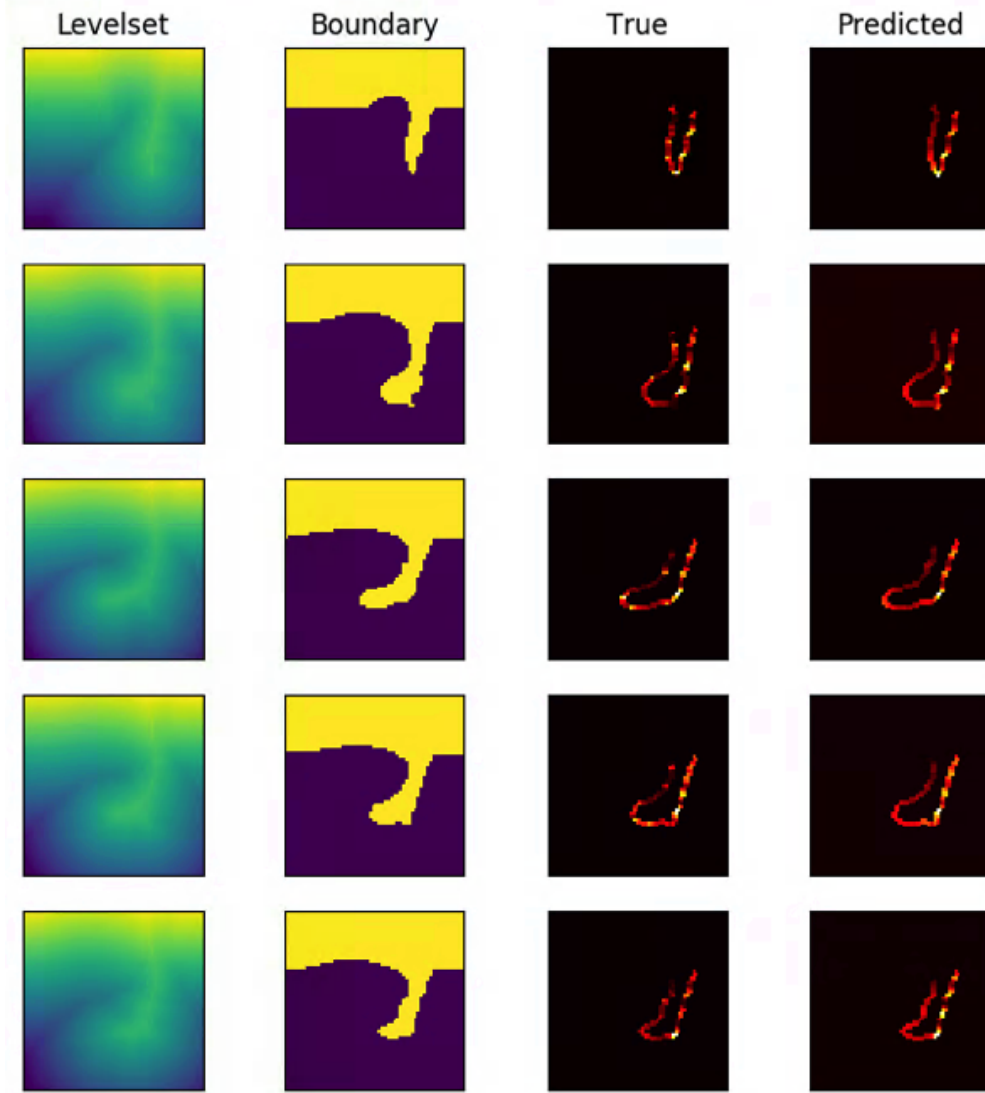


Figure 6: 5 Exemplary predictions of the testing examples compared with the corresponding true absorption distribution.

5 Future Work

The current project can be straightforwardly extended to 3D if more time is rendered. However, it is expected that the amount of data needs to be increased for 3D machine learning tasks. Moreover, the architecture of the neural network is expected to be more complex. Transfer learning (combining components of already-trained deep neural networks with customized, untrained layers) should be considered for 3D data sets.

Reference

- [1] R. Cunningham, C. Zhao, N. Parab, C. Kantzos, J. Pauza, K. Fezzaa, T. Sun, and A. D. Rollett, “Keyhole threshold and morphology in laser melting revealed by ultrahigh-speed x-ray imaging,” *Science*, vol. 363, no. 6429, pp. 849–852, 2019.
- [2] S. M. H. Hojjatzadeh, N. D. Parab, W. Yan, Q. Guo, L. Xiong, C. Zhao, M. Qu, L. I. Escano, X. Xiao, K. Fezzaa *et al.*, “Pore elimination mechanisms during 3d printing of metals,” *Nature communications*, vol. 10, no. 1, pp. 1–8, 2019.
- [3] A. A. Martin, N. P. Calta, S. A. Khairallah, J. Wang, P. J. Depond, A. Y. Fong, V. Thampy, G. M. Guss, A. M. Kiss, K. H. Stone *et al.*, “Dynamics of pore formation during laser powder bed fusion additive manufacturing,” *Nature communications*, vol. 10, no. 1, pp. 1–10, 2019.
- [4] M. Bayat, A. Thanki, S. Mohanty, A. Witvrouw, S. Yang, J. Thorborg, N. S. Tiedje, and J. H. Hattel, “Keyhole-induced porosities in laser-based powder bed fusion (l-pbf) of ti6al4v: High-fidelity modelling and experimental validation,” *Additive Manufacturing*, vol. 30, p. 100835, 2019.